

DEM analysis on CPT mechanism in pure and structured sand grounds considering various penetrated inclinations

Mingjing Jiang

Institution Department of Geotechnical Engineering/ College of Civil Engineering/Tongji University, Shanghai, China, mingjing.jiang@tongji.edu.cn

Maoyi Niu

Institution Department of Geotechnical Engineering/ College of Civil Engineering/Tongji University, Shanghai, China, 1510189@tongji.edu.cn

Fuguang Zhang

School of Civil Engineering/Shijiazhuang Tiedao University, Shijiazhuang, China

ABSTRACT: Using a novel bond contact model of structured sand, this paper presents a numerical investigation into the mechanism of cone penetration test (CPT) technique in different types of sand ground (i.e. pure sand, structured sand I/II/III) with a series of penetrated inclinations (i.e. 0° , 15° , 30° and 45°) by two-dimensional Discrete Element Method (DEM). The results show that, the evolution characteristics of normalized tip resistance as well as its components on both sides are closely related to the varied penetrated inclinations and bond strengths. As the inclination angle increases, asymmetrical distribution of contact force chain can be observed, as well as the gradual enlarged distribution of bond breakage exhibited like an inverted bell. In the inclined penetration process, the principal stresses on the left side near the penetration path always rotate clockwise, whereas those on the corresponding right side rotate clockwise firstly and then turn to rotate anticlockwise, both of which are influenced by the penetrated inclination more significantly than by the bond strength of structured sand. The penetration effect leads to the soils adjacent to the penetrometer undergo the obvious loading and unloading processes, making the higher stress level distribute widely outside the inner residual stress state range. As the penetrometer inclines, the soils on the right side near the penetrometer tends to approach its peak stress level at a shallower penetration depth than those on the corresponding left side.

Keywords: cone penetration test; Distinct Element Method; structured sand; penetrated inclination; tip resistance

1. Introduction

The cone penetration test (CPT) is a reliable in-situ testing technique to obtain the soil stratifications and mechanical properties [1-3] in geotechnical engineering. Many investigations have been performed on the vertical CPT mechanism on clay, sand and lunar soil using a variety of approaches, including the theoretical analyses (i.e. bearing capacity theory [4] and cavity expansion theory [5]), experiments (i.e. laboratory chamber calibration tests [6, 7] and centrifuge tests [8, 9]) and numerical analyses (i.e. finite element method (FEM) [10-14] and distinct element method (DEM) [15-19]). Moreover, in recent years, some researchers attempted to deal with more challenging problems existed in the vertical CPT technique, i.e. the suction effect of unsaturated soils [20, 21], the irregular particle shape effect [22] and the crushability effect of soils [23].

In addition, due to the complicated geological conditions like inclined sedimentation, the existing structures or lack of access in site surveys, the CPT technique is necessary to be performed in various inclinations, which is not an axisymmetric boundary problem in most cases. A few researchers have tried to explore the inclined penetration mechanism using the above approaches by several aspects, i.e. relationship of tip resistance between horizontal and vertical CPTs [24], the effect of soil anisotropy [25, 26], penetration characteristics in lunar soil [27] and the effect of penetrometer-soil fric-

tion under different inclinations [28]. However, the investigations on the inclined CPT technique still remain insufficient, especially the penetration mechanism in natural sand ground under different inclinations. It is well known that the natural sands are micro-structured and characterized with notable inter-particle bonding due to the effects of sedimentary environment and stress history. Therefore, DEM provides an alternative tool to interpret the penetration mechanism and observe the whole penetration process in natural sand, which can give insight into the mechanical behavior of granular material both at microlevel and macrolevel.

Considering the micro characteristics of natural sand, this paper presents a numerical investigation into the inclined penetration mechanism in pure and structured sand grounds by two-dimensional Discrete Element Method (DEM). With the use of a micro bond contact model proposed for structured sand, four sand types were calibrated, three of which are structured sands characterized with different bond strengths, and the other is pure sand for comparison. Then a series of CPTs with different inclinations (i.e. 0° , 15° , 30° and 45°) were numerically performed on the four types of sand grounds. The penetration mechanism was discussed in detail by investigating the evolutions of normalized tip resistance, distributions of contact force chain, bond breakage field, rotation of principal stresses and characteristics of stress level during the penetration process.

2. Bond contact model of structured sand

Based on the scanning electric microscopic analysis of structured sand [29], a conceptual 2D micro bond contact model considering two bond modes can be established [30]. The mode A represents that the bonds are formed in the inter-particle voids with a certain bond thickness, and thus two particles are separated by bond. By contrast, the mode B represents that two particles are contacted directly so that the bonds are formed around the contact regions [31]. For a pair of particles with radii R_1 and R_2 , the bond can be generated when h_{min} at contact is no more than the critical bond thickness h_{max}^{cr} , and the bond width B can be calculated automatically by the following Eq. (1) [30]:

$$B = \sqrt{4\bar{R}^2 - (2\bar{R} + h_{min} - h_{max}^{cr})^2} \quad (1)$$

where the common radius $\bar{R} = 2R_1R_2 / (R_1 + R_2)$.

The mechanical response of the bond contact model with two modes can be unified. On one hand, the inter-particle mechanical response is activated once $h_{min}=0$ or bond is broken, following the classic inter-particle rolling resistance model [32]. On the other hand, based on the bond rolling resistance model [33], the mechanical response of bond in three directions, i.e. normal, tangential and rolling directions, can be described in an elastobrittle-plastic residual way.

Fig. 1. presents the adopted strength envelope in a three-dimensional space, where the red section represents the peak bond strength corresponding to the critical state and the blue section represents the residual bond strength due to friction and bond shape existed in the compressive zone. As the projection of strength envelope, the bond failure criterion in the shear bond force F_s^b - bond moment M^b plane can be approximated as an ellipse and described by the following Eq. (2), which varies in size with normal bond force F_n^b :

$$\left(\frac{F_s^b}{R_{sb}} \right) + \left(\frac{M^b}{R_{rb}} \right) \begin{cases} < 1 & \text{(intact bond)} \\ = 1 & \text{(critical state)} \\ > 1 & \text{(broken bond)} \end{cases} \quad (2)$$

where R_{sb} is the shear strength of bond under compression (tension) - shear condition, and R_{rb} is the rolling strength of bond under compression (tension) - rolling condition, both of which can be expressed as the functions of F_n^b , the compressive and tensile strength of bond R_{cb} and R_{tb} [30].

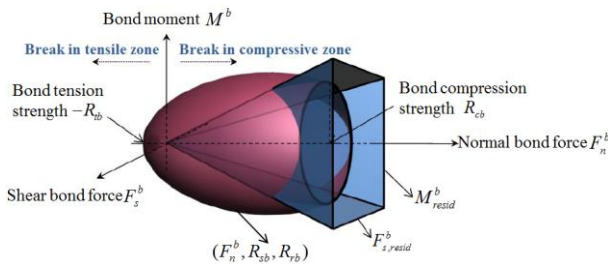


Figure 1. 3D bond strength envelope of the bond contact model [30].

3. DEM modeling of CPT

3.1. Ground generation

Using the multilayer under-compaction method [34], the homogeneous sand ground was generated by compacting eight layers of particles to the target void ratio of 0.27, and then subjected to an amplified gravity field of 5g to simulate the deep ground condition. The contact bonds were assigned finally with the parameters illustrated in Table 1., whose initial total number is 711799. As shown in Fig. 2., the final size of the ground model is 6m wide and 2.75m high. The sand ground was composed of 298550 particles with the diameters uniformly ranging between 6 and 9 mm given a mean diameter d_{50} of 7.6mm, and the particle density was set to be 2600kg/m³. As illustrated in Table 1., to analyze the bond effect of structured sand on the penetration mechanism, four types of sand were considered, i.e. pure sand and structured sand I/II/III, which have different bond strengths while identical frictional parameters. Based on a series of biaxial compression test simulations with the strain rate of 5%/min, the macro calibrated parameters of four sand types were obtained, as presented in Table 1., including the distinct cohesion c and the similar internal frictional angle φ . Except for the bond strength effect, the effect of penetrated inclination was also investigated by considering four inclination angles (i.e. 0°, 15°, 30° and 45°). Here, the inclination angle is defined as the vertical direction to the central axis of the penetrometer. Figs. 2-3. only present the DEM model and the corresponding layouts respectively in the inclination of 30°, to which other inclinations are similar and thus are not given. To sum up, sixteen CPT programs were performed numerically in this paper, including different combinations of sand type and penetrated inclination.

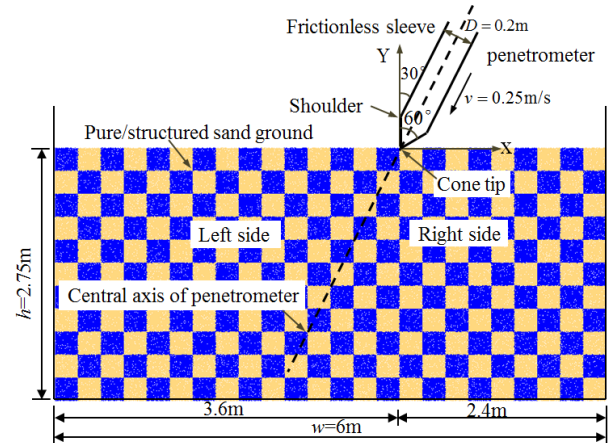


Figure 2. DEM model of CPT with the inclination of 30°.

Table 1. Model parameters used in DEM simulations

Inter-particle frictional coefficient μ^p	0.5
Inter-particle rolling resistance coefficient β^p	1.4
Normal contact stiffness of particle k_n^p (N/m)	2.0×10^8
Tangential contact stiffness of particle k_s^p (N/m)	1.5×10^8
Frictional coefficient of bond μ^b	/ (pure), 0.5(I, II, III)
Critical bond thickness h_{max}^{cr} (m)	/ (pure), 0.0013(I,II,III)
Elastic modulus of bond E_b (kPa)	/ (pure),

	5×10^5 (I,II,III)
Tensile strength of bond R_{tb} (N/m)	/ (pure), 6.0×10^4 (I), 8.6×10^4 (II), 1.1×10^5 (III)
Compressive strength of bond R_{cb} (N/m)	/ (pure), 1.3×10^6 (I), 1.75×10^6 (II), 2.3×10^6 (III)
Frictional coefficient between wall and particle	0
Normal contact stiffness of wall k_n^w (N/m)	1.5×10^9
Tangential contact stiffness of wall k_t^w (N/m)	1.0×10^9
Calibrated cohesion c (kPa)	0 (pure), 25.2 (I), 48.6 (II), 66.2 (III)
Calibrated internal frictional angle ϕ (°)	30.21 (pure), 31.07 (I), 30.86 (II), 31.15 (III)

3.2. Layout of penetrometer and measurement circles

After the sand ground was generated, a standard penetrometer was created above the ground and some necessary factors were considered in choosing the sizes of the penetrometer. The diameter of the penetrometer D was set to 0.2m, and thus the value of $D/d_{50} = 26.3 > 20$, which can ensure that the cone tip face can be always in contact with more than 13 particles and thus acceptable rational steady values of tip resistance can be provided [35, 36]. As aforementioned, the sand ground was 6m in width, resulting in a value of $w/R = 60 > 40$, which can reduce the possible boundary effect [35]. Moreover, considering the boundary effect in the inclined penetration process, the penetrometer in each case was generated at a distance of 3.6m from the left boundary, which slightly deviated from the symmetrical axis, as presented in Fig. 2.. The penetrometer was moved downward at a constant rate of 0.25m/s along the central axis of the penetrometer, which is a relatively high penetration rate to reduce the computational time and meanwhile not affect the CPT simulation results significantly [37]. For simplification, the frictional coefficient between penetrometer and sand was set to 0.0 to simulate a perfectly smooth condition.

In addition, as presented in Fig. 3., to capture the features of stress variation of soils adjacent to the penetrometer, 32 measurement circles with the diameter of 0.12m were arranged at different depths along the central axis of the penetrometer, each containing about 200 particles, and thus the evolutions of stress rotation and stress level would be traced as the cone penetration proceeds.

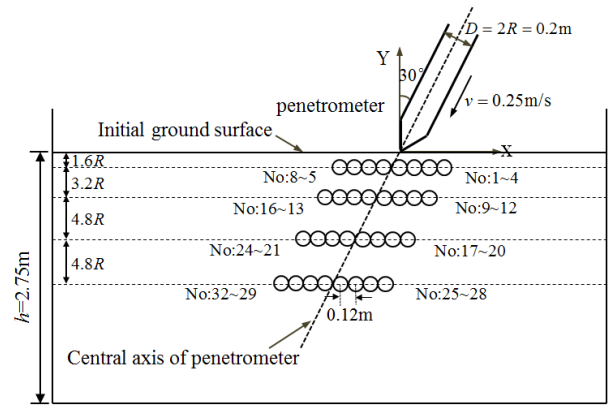


Figure 3. Layout of penetrometer and measurement circles in the CPT model with the inclination of 30°

4. Analyses of simulation results

Sixteen simulated cases would be carried out with combination of four sand types and four penetrated inclinations. In this section, the analyses of different penetration inclinations provided below are based on the case of structured sand I, while the comparisons of different bond strengths are mainly based on the inclination of 30° or 45°. Those in other cases not given are of the similar characteristics.

4.1. Tip resistance

The tip resistance q_c is defined as the summation of the contact force components exerted on the tip parallel to the central axis of the penetrometer divided by the penetrometer diameter D , which is composed of the tip resistance components acting on the left and right sides of tip identified as $q_{c,left}$ and $q_{c,right}$ respectively, as calculated in the following Eq. (3):

$$q_c = q_{c,left} + q_{c,right} = \frac{F_{left} + F_{right}}{D} \quad (3)$$

where F_{left} and F_{right} correspond to the summation of contact force component exerted on the left and right side of tip parallel to the central axis of penetrometer respectively. In this paper, the tip resistance and its components on both sides were all normalized by the initial vertical stress $\sigma_{v,ini}$, which would be adopted in the following analyses.

Note that, although all the curves in Fig. 4. and Fig. 5. exhibit some noisy response, their main features are consistent with those observed in centrifuge modelling [35]. Fig. 4. shows that, as the cone penetration proceeds, the normalized tip resistance $q_c / \sigma_{v,ini}$ in each case all surges to the peak value, then decreases gradually and finally approaches the steady constant value, which was described as three phases called by shallow penetration, deep penetration-1 and deep penetration-2 respectively in previous study [36]. As illustrated in Fig. 4(a)., for each type of sand ground, the peak value of $q_c / \sigma_{v,ini}$ increases and its corresponding penetration depth slightly decreases as the inclination angle increases. Moreover, it can be seen that, the steady state of deep penetration-2 has been reached at the depth of $y/R=12-15$ with the inclinations of 0° and 15°, which

seems to be reached until y/R increases to 18-20 at the larger inclinations of 30° and 45° . Hence, the more the penetrometer inclines, the deeper the deep penetration-1 phase extends, whereas the steady values of $q_c / \sigma_{v,ini}$ at different inclinations are almost the same. By contrast, as presented in Fig. 4(b)., for each penetrated inclination, the peak and steady values of $q_c / \sigma_{v,ini}$ all increase with the increase of bond strength. However, the bond strength of structured sand seems to have little effect on the depth of transition between shallow and deep penetration-1, as well as on the depth corresponded to the steady state of deep penetration-2.

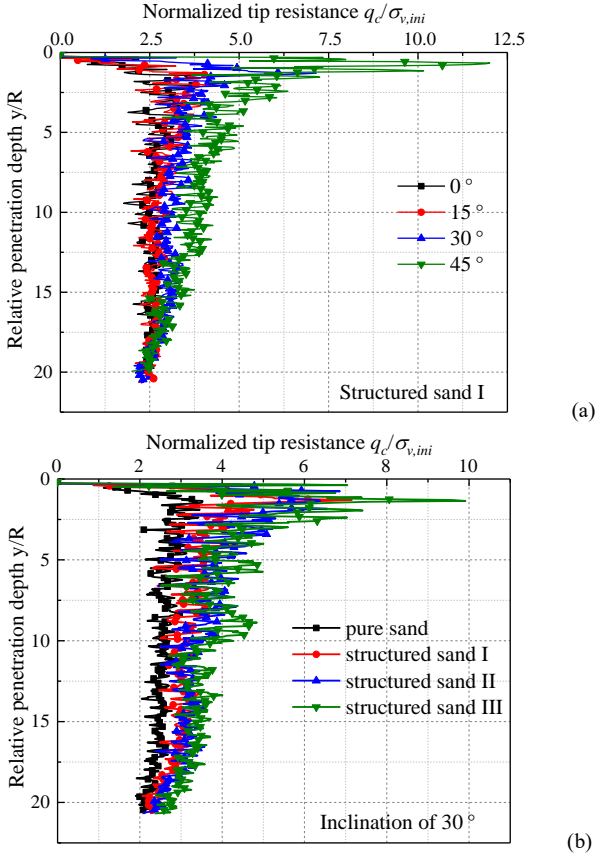


Figure 4. The normalized tip resistance against relative penetration depth: (a) in structured sand I ground with different penetrated inclinations; (b) in different types of sand ground with the inclination of 30° .

In addition, it is necessary to analyze the normalized tip resistance components $q_{c,left} / \sigma_{v,ini}$ and $q_{c,right} / \sigma_{v,ini}$ in the inclined penetration process, which are under asymmetric stress states and exhibit different evolution characteristics in comparison with the vertical penetration. Fig. 5. provides the evolutions of $q_{c,left} / \sigma_{v,ini}$ and $q_{c,right} / \sigma_{v,ini}$ in structured sand I ground with each penetrated inclination. It can be observed from Fig. 5. that, in the inclined penetration, $q_{c,left} / \sigma_{v,ini}$ has no distinct decrease stage and approaches the steady constant value preceded $q_{c,right} / \sigma_{v,ini}$. As the inclination angle increases, the steady value of $q_{c,left} / \sigma_{v,ini}$ decreases while its corresponding penetration depth increases (Fig. 5(a)). By contrast, comparing Fig. 5(b). with Fig. 4(a)., it can be seen that, the evolution characteristic of

$q_{c,right} / \sigma_{v,ini}$ with the varied inclinations is the same as that $q_c / \sigma_{v,ini}$ exhibits, as elaborated above. Moreover, as the penetrometer gradually inclines, $q_{c,right} / \sigma_{v,ini}$ tends to be larger than $q_{c,left} / \sigma_{v,ini}$ and more predominant in $q_c / \sigma_{v,ini}$, while the steady constant values of two components seem to be closed.

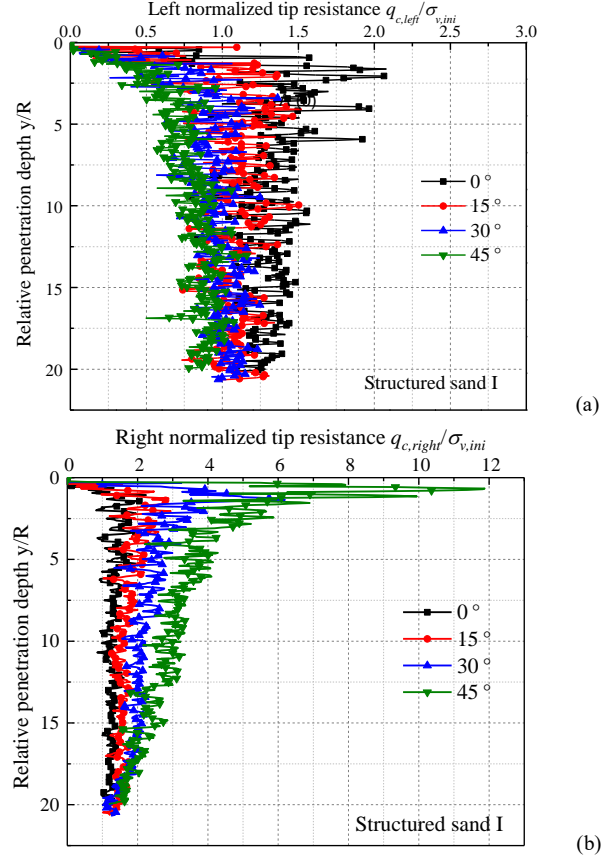


Figure 5. The evolutions of normalized tip resistance components in structured sand I ground with different inclinations: (a) the left side component; (b) the right side component.

4.2. Distributions of contact force chain and bond breakage

Fig. 6. and Fig. 7. provide the distributions of contact force chain and total bond breakage respectively at the relative penetration depth y/R of 15 in structured sand I ground under each inclination. In Fig. 6. and Fig. 7., the black line and spot represent the extension of contact force chain and the location of bond breakage respectively, and the thicker the black line is (the more intensive the black spot is), the larger the contact force is (the more the bond breakage number is). As presented in Fig. 6., in different penetrated inclinations, the dense distribution of contact force chain can always be observed beneath the cone tip along the central axis of penetrometer. Besides that, when the cone penetration proceeds vertically, the contact force chains are concentrated symmetrically on both sides of the cone tip, while those near the penetrometer sleeves are sparse. As the penetrometer gradually inclines, the contact force chains tend to be asymmetrically distributed, which exhibit to be much denser on the right sides of cone tip and sleeve than those on the corresponding left sides.

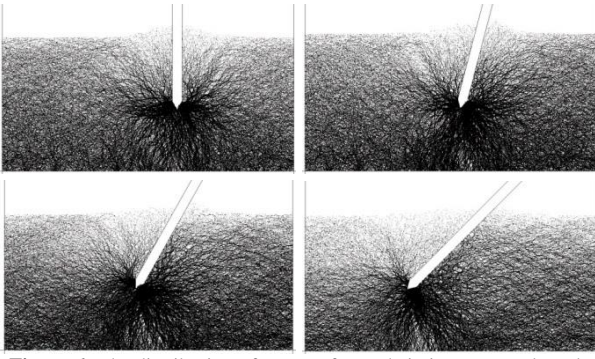


Figure 6. The distribution of contact force chain in structured sand I ground at $y/R=15$ with the inclination of: (a) 0° ; (b) 15° ; (c) 30° ; (d) 45° .

Correspondingly, from Fig. 7. it can be observed that, in the vertical penetration, most of the bond breakages are distributed symmetrically on both sides of the penetrometer as well as beneath the tip point, which approximately exhibits to be an inverted bell profile. As the penetration direction changes gradually from a vertical direction to 45° , the inverted bell-shaped concentrated distribution of bond breakages is enlarged, and its vertex region tends to move left gradually. As shown in Figs. 7(b)-(d)., for the inclined penetration, the soil on the left side of the penetrometer tends to heave and its bond breakage range is extended horizontally, in which several failure surfaces nearly perpendicular to the penetrometer sleeve can be observed. By contrast, the soil on the right side of the penetrometer mainly experiences compression and its corresponding bond breakage range extends outwards in a direction perpendicular to the penetrated inclination.

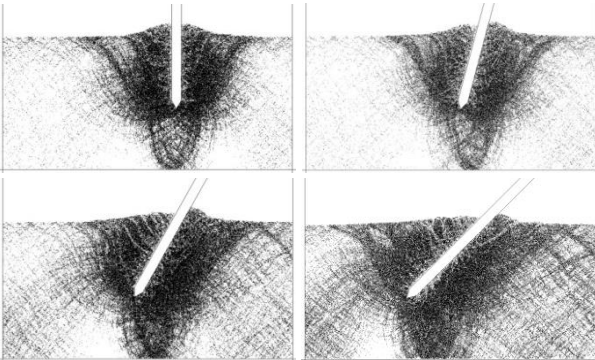
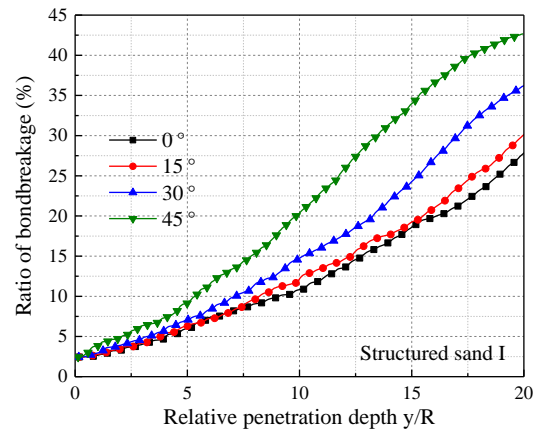
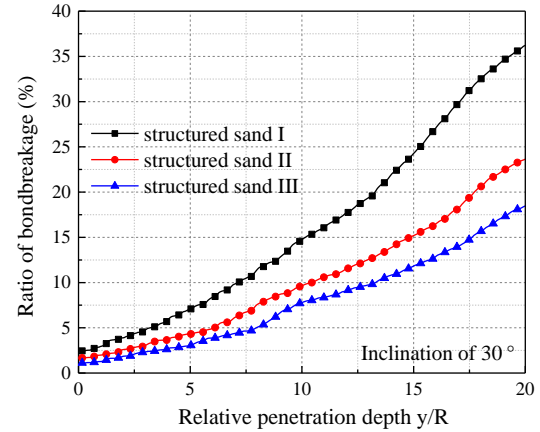


Figure 7. The distribution of bond breakage in structured sand I ground at $y/R=15$ with the inclination of: (a) 0° ; (b) 15° ; (c) 30° ; (d) 45° .

In addition, to analyze the evolutions of bond breakages quantitatively, the bond breakage ratio is traced in each case, which is defined as the ratio of bond breakage number and total bond number, as illustrated in Fig. 8.. It indicates that the cumulative bond breakage ratio gradually increases in each case as the penetration proceeds. Fig. 8. presents that, the more the penetrometer inclines, the larger the bond breakage ratio is at the same penetration depth, while the bond breakage ratio tends to decrease with the increase of bond strength.



(a)



(b)

Figure 8. The bond breakage ratio against y/R : (a) in structured sand I ground with different penetrated inclinations; (b) in different structured sand grounds with the inclination of 30° .

4.3. Rotation of principal stress

Figs. 9-11. provide the rotations of principal stresses at the observed locations in different cases, in which a positive angle represents an anticlockwise rotation and vice versa. As presented in Fig. 9., during the whole vertical penetration process, the rotations of principal stresses on both sides of the central axis of penetrometer are nearly symmetrical, and all experience the rotations as large as 180° approximately. That is, initially the penetration effect on the deeper observed points (i.e. $y/R=4.8, 9.6$ and 14.4) is slight, where the directions of principal stresses are predominantly controlled by gravity and scarcely rotates. As the tip approaches the deeper observed points, the obvious clockwise and anticlockwise rotation of principal stress can be observed respectively at the left and right observed points, and approaches 60° nearly, meaning that the major principal stresses tend to be perpendicular to the tip faces. When the tip moves downwards and far away from the observed points, the principal stresses continue rotating and nearly go back to the vertical direction finally.

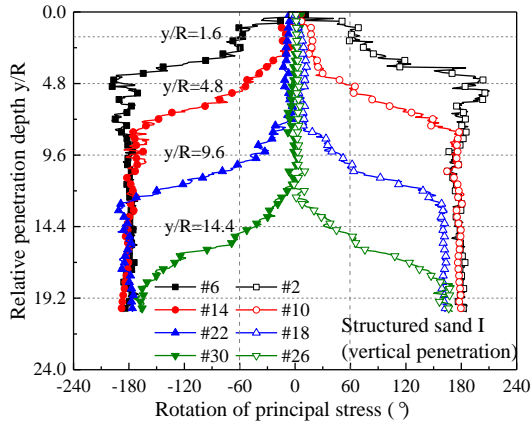
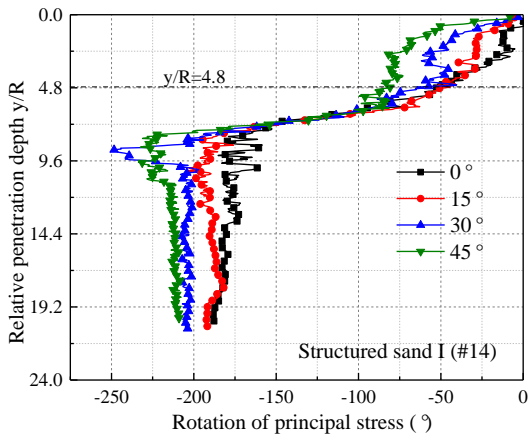
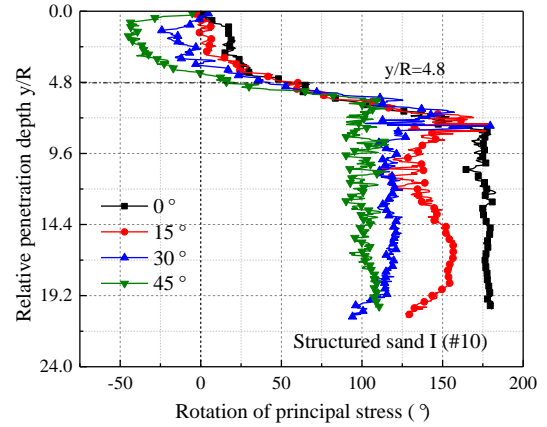


Figure 9. Rotation of principal stress at different observed points in structured sand I ground with the vertical penetration.

By contrast, during the inclined penetration process, the principal stresses exhibit asymmetric rotation characteristics on both sides adjacent to the penetrometer, and the experienced stress rotations at the left observed points are much larger than those at the corresponding right ones, as illustrated in Fig. 10. and Fig. 11.. As the inclined penetrometer moves towards, approaches and passes over the observed points gradually, the rotations of principal stresses on both sides near the central axis of the penetrometer are affected by the penetrated inclination firstly, then turn to be predominantly controlled by the penetration effect of the tip and finally tend to be influenced by the penetrometer side again. Hence, the principal stresses at the left observed points always rotate clockwise, whereas those at the right observed points rotate clockwise firstly to be parallel to the penetration direction and then turn to rotate anticlockwise. In addition, it can be seen from Fig. 10. that, at the left observed points, the rotation corresponded to the approach of the penetrometer and the final constant rotation of stress increases with the increase of inclination angle. While at the right observed points, the maximum clockwise rotation increases and the final constant rotation decreases as the penetrated inclination increases gradually. For different sand types, it seems that the bond strength only affects the final constant values of stress rotation obviously, exhibiting that the maximum rotations on both observed sides in pure sand ground are larger than those in structured sand ground, as presented in Fig. 11..

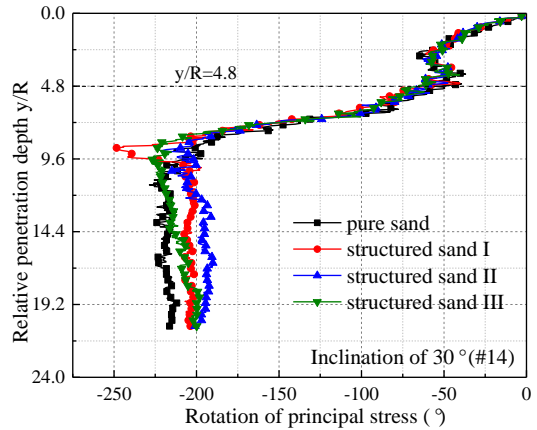


(a)

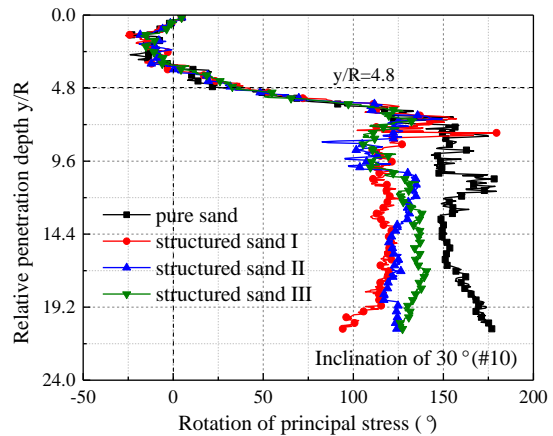


(b)

Figure 10. Rotation of principal stress in structured sand I ground with different inclinations: (a) at the left observed point of 14; (b) at the right observed point of 10.



(a)



(b)

Figure 11. Rotation of principal stress in different types of sand ground with the inclination of 30°: (a) at the left observed point of 14; (b) at the right observed point of 10.

4.4. Stress level

To analyze the stress variations and the damage extent comprehensively in the soil adjacent to the penetrometer as the penetration proceeds, the stress level S is adopted in this paper, which is defined as the following Eq. (4):

$$S = \frac{\sigma_1 - \sigma_3}{(\sigma_1 - \sigma_3)_f} = \frac{\sigma_1 - \sigma_3}{\sigma_3 \cdot \tan^2\left(45^\circ + \frac{\varphi}{2}\right) + 2c \cdot \tan\left(45^\circ + \frac{\varphi}{2}\right) - \sigma_3} \quad (4)$$

where σ_1 and σ_3 correspond to the major and minor principal stress respectively. The calibrated values of cohesion c and internal frictional angle φ of each sand

type were used as elaborated in Table 1..

Fig. 12. provides the stress level variations of the soils at the observed locations (i.e. 10, 14, 18 and 22) in the inclinations of 0° and 45° respectively, which can reflect the characteristics of stress path in a quantitative way. Fig. 12. presents that, with the increasing penetrated depth, the stress levels increase to the peak gradually when the cone tip approaches toward the observed depth, then decrease and fluctuate at the residual constants when the tip moves downwards and away from the observed location. The phenomenon indicates that the penetration leads to the soil near the penetrometer undergoing the evident loading and unloading processes between the peak and residual strength envelopes, as previously investigated [36]. Moreover, in the vertical penetration, the soil on the left and right sides of the penetrometer at the same depth approach the peak stress state simultaneously, as presented in Fig. 12(a).. By contrast, with the penetrometer gradually inclines, the soil on the right side tends to approach its peak stress state little earlier than that on the corresponding left side, for example in the inclination of 45° (Fig. 12(b)).

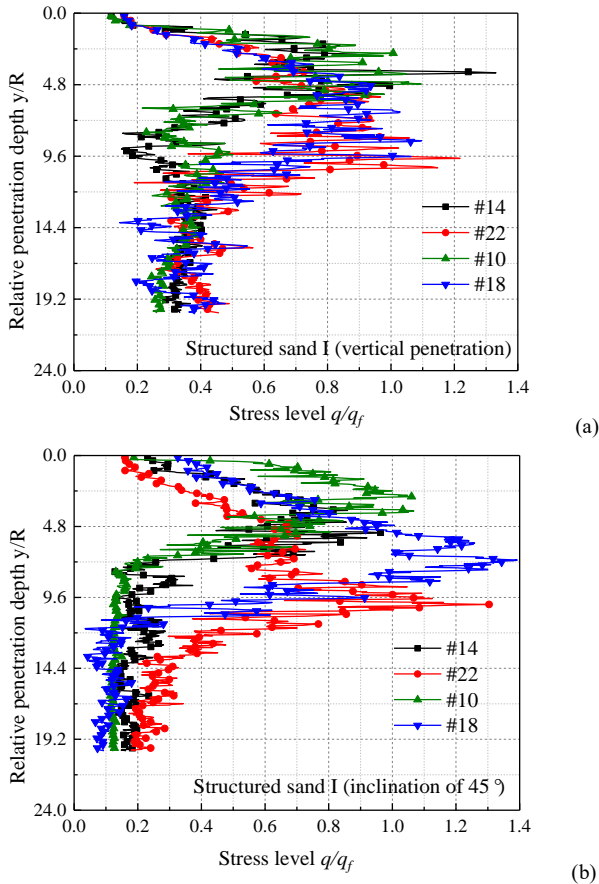


Figure 12. The evolution of stress level at the observed points of 10, 14, 18 and 22 in structured sand I ground: (a) with vertical penetration; (b) with the inclination of 45° .

In addition, in order to describe the features of stress level visually during the penetration process in the whole sand ground, the stress level fields in structured sand I ground with the inclination of 30° at different y/R are given, as presented in Fig. 13.. The stress level of the soil adjacent to the penetrometer is relatively low in each case, showing again an inverted bell profile, which seems to be partly consistent with the concentrated distribution of bond breakage. It can be deduced that, as

the penetration proceeds, the soils adjacent to the penetrometer tip and sleeve undergo the obvious loading process and increase to the peak stress level firstly, leading to the numerous bond breakages and some minute failure surfaces. Then, the soil near the penetrometer is stress-released and unloaded to the residual stress state. Finally, the penetration effect extends outwards continually, making the higher stress level distributions of the soil outside the inverted bell-shaped range of inner soil at the residual stress state, especially of the soil ahead of the penetration path. Moreover, it can be seen from Fig. 13. that, the deeper the penetration proceeds, the wider the high stress level distributions are extended at each inclination.

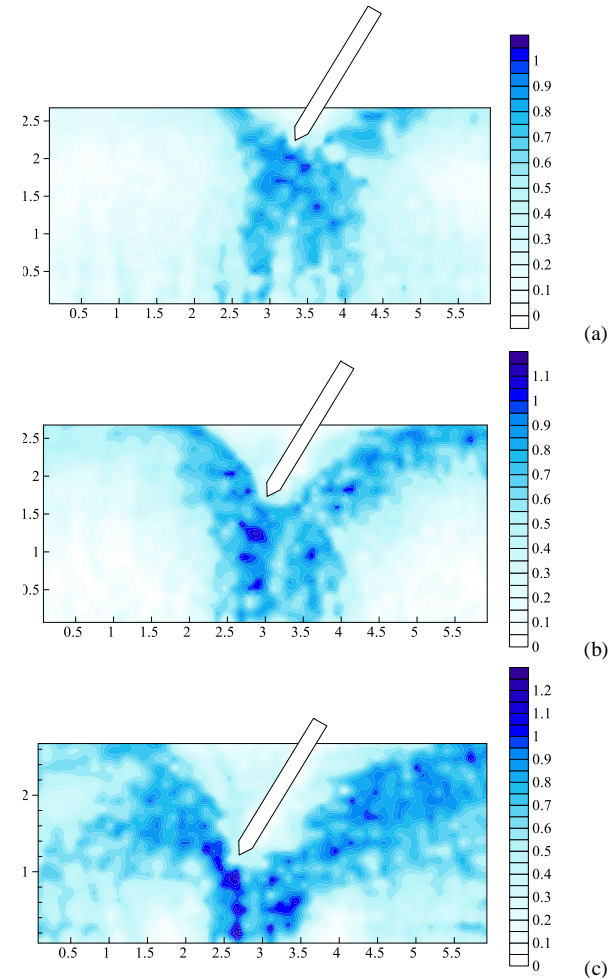


Figure 13. Stress level field in structured sand I ground with the inclination of 30° : (a) at $y/R=5$; (b) at $y/R=10$; (c) at $y/R=15$.

From Fig. 12. and Fig. 13., it can be noted that, the stress level of the soil at the peak stress state may exceed 1.0 slightly in the penetration process, meaning that the soil arrives over the peak strength envelope slightly. This phenomenon appears not to be unreasonable and can be explained by the rate-dependent behavior of soil [15, 37]. That is, the strain rate the soil has undergone in the numerical CPTs, which depends on the relative position of soil to the penetrometer and varies with the penetration process, may not be always the same as the one used in the biaxial compression test simulations from which the peak stresses were obtained.

5. Conclusions

With the use of novel bond contact model, this paper presents a study on the penetration mechanism considering the varied penetrated inclinations and bond strengths of sand from the viewpoints of tip resistance, contact force chain, bond breakage, stress rotation and stress level via DEM simulations. The main conclusions are as follows:

- (1) The evolution characteristics of $q_c / \sigma_{v,ini}$ and its components on both sides, including its peak value, steady constant value and the depth that the shallow penetration and deep penetration-1 approaches respectively, are influenced by the penetrated inclination and the bond strength of the sand.
- (2) The contact force chain tends to be distributed asymmetrically in the inclined penetration, which is more concentrated on the right sides of cone tip and sleeve. The inverted bell-shaped concentrated distribution of bond breakage can be observed in each inclination, which enlarges as the penetrometer inclines.
- (3) During the inclined penetration, the principal stresses on the left side adjacent to the penetrometer always rotate clockwise, whereas those on the corresponding right side rotate clockwise initially to approach the penetrated direction and then anti-clockwise. The penetrated inclination affects the rotation characteristics more significantly than the bond strength of sand.
- (4) The increase of penetrated inclination makes the corresponding depth of peak stress level on the right side near the penetrometer slightly deeper than that on the left side. The penetration effect leads to the obvious loading and unloading processes in the soils adjacent to the penetrometer tip and sleeve whose region is also like an inverted bell, and thus makes the higher stress level distribute widely outside.

This paper mainly investigates the effect of bond strength of structured sand in several penetrated inclinations, the effect of other factors like the frictional sleeve and the varied frictional properties of structured sand is worthy to be studied in the future.

Acknowledgement

The project presented in this article is supported by the National Natural Science Foundation of Grant Nos. 51639008 and 51890911, all of which are sincerely appreciated.

References

- [1] Wang, Y., Huang, K., Cao, Z. J. "Probabilistic identification of underground soil stratification using cone penetration tests", Canadian Geotechnical Journal, 50(7), pp. 766-776, 2013. <https://doi.org/10.1139/cgj-2013-0004>
- [2] Robertson, P. K. "CPT-based Soil Behaviour Type (SBT) Classification System - an update", Canadian Geotechnical Journal, 53(12), pp. 1910-1927, 2016. <https://doi.org/10.1139/cgj-2016-0044>
- [3] Sadrekarimi, A. "Estimating relative density of sand with cone penetration test", Proceedings of the Institution of Civil Engi-

- neers Ground Improvement, 169(4), pp. 1-11, 2016. <https://doi.org/10.1680/jgrim.15.00017>
- [4] Durgunoglu, H.T., Mitchell, J.K. "Static penetration resistance of soils", In: Proceedings of the ASCE Specialty Conference on In-Situ Measurements of Soil Properties, California, United States, 1975, pp. 151-189.
- [5] Salgado, R., Mitchell, J. K., Jamiolkowski, M. "Cavity expansion and penetration resistance in sand", Journal of Geotechnical and Geoenvironmental Engineering, 123(4), pp. 344-354, 1997. [https://doi.org/10.1061/\(ASCE\)1090-0241\(1997\)123:4\(344\)](https://doi.org/10.1061/(ASCE)1090-0241(1997)123:4(344))
- [6] Houlsby, G. T., Hitchman, R. "Calibration chamber tests of a cone penetrometer in sand", G ́otechnique, 38(1), pp. 39-44, 1988. <https://doi.org/10.1680/geot.1988.38.1.39>
- [7] Arshad, M. I., Tehrani, F.S., Prezzi, M., Salgado, R. "Experimental study of cone penetration in silica sand using digital image correlation", G ́otechnique, 64(7), pp. 551-569, 2014. <https://doi.org/10.1680/geot.13.P.179>
- [8] Bolton, M.D., Gui, M. W., Garnier, J., Corte, J. F., Bagge, G., Laue, J., Renzi, R. "Centrifuge cone penetration tests in sand", G ́otechnique, 49(4), pp. 543-552, 1999. <https://doi.org/10.1680/geot.1999.49.4.543>
- [9] Liu, Q. B., Lehane, B. M. "The influence of particle shape on the (centrifuge) cone penetration test (CPT) end resistance in uniformly graded granular soils", G ́otechnique, 62(11), pp. 973-984, 2012. <https://doi.org/10.1680/geot.10.P.077>
- [10] Huang, W. X., Sheng, D. C., Sloan, S. W., Yu, H. S. "Finite element analysis of cone penetration in cohesionless soil", Computers and Geotechnics, 31, pp. 517-528, 2004. <https://doi.org/10.1016/j.compgeo.2004.09.001>
- [11] Lu, Q., Randolph, M. F., Hu, Y., Bugarski, I. C. "Numerical study of cone penetration in clay", G ́otechnique, 54(4), pp. 257-267, 2004. <https://doi.org/10.1680/geot.54.4.257.36358>
- [12] Liyanapathirana, D. S. "Arbitrary Lagrangian Eulerian based finite element analysis of cone penetration in soft clay", Computers and Geotechnics, 36(5), pp. 851-860, 2009. <https://doi.org/10.1016/j.compgeo.2009.01.006>
- [13] Tolooiyani, A., Gavin, K. "Modelling the Cone Penetration Test in sand using Cavity Expansion and Arbitrary Lagrangian Eulerian Finite Element Methods", Computers and Geotechnics, 38(4), pp. 482-490, 2011. <https://doi.org/10.1016/j.compgeo.2011.02.012>
- [14] Kouretzis, G. P., Sheng, D. C., Wang, D. "Numerical simulation of cone penetration testing using a new critical state constitutive model for sand", Computers and Geotechnics, 56, pp. 50-60, 2014. <https://doi.org/10.1016/j.compgeo.2013.11.002>
- [15] Jiang, M. J., Harris, D., Zhu, H. H., "Future continuum models for granular materials in penetration analyses", Granular Matter, 9(1), pp. 97-108, 2007. <https://doi.org/10.1007/s10035-006-0026-y>
- [16] Jiang, M. J., Zhu, H. H., Harris, D. "Classical and non-classical kinematic fields of two-dimensional penetration tests on granular ground by Discrete Element Method analyses", Granular Matter, 10(6), pp. 439-455, 2008. <https://doi.org/10.1007/s10035-008-0107-1>
- [17] Jiang, M. J., Liu, F., Wang, H. N., Wang, X. X. "Investigation of the effect of different gravity conditions on penetration mechanisms by the Distinct Element Method", Engineering Computations, 32(7), pp. 2067-2099, 2015. <https://doi.org/10.1108/EC-07-2014-0153>
- [18] Arroyo, M., Butlanska, J., Gens, A., Calvetti, F., Jamiolkowski, M. "Cone penetration tests in a virtual calibration chamber", G ́otechnique, 61(6), pp. 525-531, 2011. <https://doi.org/10.1680/geot.9.P.067>
- [19] Ecemis, N., Bakunowicz, P. "Feasible packing of granular materials in discrete-element modelling of cone-penetration testing", Geomechanics and Geoenvironment, 13(3), pp. 198-216, 2018. <https://doi.org/10.1080/17486025.2018.1435912>
- [20] Miller, G. A., Tan, N. K., Collins, R. W., Muraleetharan, K. K. "Cone penetration testing in unsaturated soils", Transportation Geotechnics, 17, pp. 85-99, 2018. <https://doi.org/10.1016/j.trgeo.2018.09.008>
- [21] Jarast, P., Ghayoomi, M. "Numerical modeling of cone penetration test in unsaturated sand inside a calibration chamber", International Journal of Geomechanics, 18(2), pp. 04017148, 2018. [https://doi.org/10.1061/\(ASCE\)GM.1943-5622.0001052](https://doi.org/10.1061/(ASCE)GM.1943-5622.0001052)
- [22] Falagush, O., McDowell, G. R., Yu, H. S. "Discrete element modeling of cone penetration tests incorporating particle shape and crushing", International Journal of Geomechanics, 15(6), pp.

04015003, 2015. [https://doi.org/10.1061/\(ASCE\)GM.1943-5622.0000463](https://doi.org/10.1061/(ASCE)GM.1943-5622.0000463)

- [23] Ciantia, M. O., Arroyo, M., Butlanska, J., Gens, A. "DEM modelling of cone penetration tests in a double-porosity crushable granular material", *Computers and Geotechnics*, 73, pp. 109-127, 2016. <https://doi.org/10.1016/j.compgeo.2015.12.001>
- [24] Broere, W., van Tol, A. F. "Horizontal cone penetration testing", *Geotechnical Site Characterization*, pp. 989-994, 1998. <https://doi.org/10.1.1.487.2860>
- [25] Wei, L., Abufarsakh, M. Y., Tumay, M. T. "Finite-element analysis of inclined piezocone penetration test in clays", *International Journal of Geomechanics*, 5(3), pp. 167-178, 2005. [https://doi.org/10.1061/\(ASCE\)1532-3641\(2005\)5:3\(167\)](https://doi.org/10.1061/(ASCE)1532-3641(2005)5:3(167))
- [26] Wei, L., Tumay, M. T., Abufarsakh, M. Y. "Field testing of inclined cone penetration", *Geotechnical Testing Journal*, 28(1), pp. 31-41, 2005. <https://doi.org/10.1520/GTJ12541>
- [27] Jiang, M. J., Wang, X. X. "不同贯入倾角下 TJ-1 模拟月壤静力触探模型箱试验研究", (Investigation of TJ-1 lunar soil simulant cone penetration tests by calibration chamber under different penetration angles) *Chinese Journal of Geotechnical Engineering*, 35(8), pp. 1442-1450, 2013. (in Chinese)
- [28] Jiang, M. J., Dai, Y. S., Cui, L., Shen, Z. F., Wang, X. X. "Investigating mechanism of inclined CPT in granular ground using DEM", *Granular Matter*, 14(5), pp. 785-796, 2014. <https://doi.org/10.1007/s10035-014-0508-2>
- [29] Cuccovillo, T., Coop, M. R. "Yielding and pre-failure deformation of structured sands", *Géotechnique*, 47(3), pp. 491-508, 1997. <https://doi.org/10.1680/geot.1997.47.3.491>
- [30] Jiang, M. J., Fu, C., Cui, L., Shen, Z. F., Zhu, F. Y. "DEM simulations of methane hydrate exploitation by thermal recovery and depressurization methods", *Computers and Geotechnics*, 80, pp. 410-426, 2016. <https://doi.org/10.1016/j.compgeo.2016.05.011>
- [31] Jiang, M. J., Sun, Y. G., Li, L. Q., Zhu, H. H. "Contact behavior of idealized granules bonded in two different interparticle distances: An experimental investigation", *Mechanics of Materials*, 55, pp. 1-15, 2012. <https://doi.org/10.1016/j.mechmat.2012.07.002>
- [32] Jiang, M. J., Yu, H. S., Harris, D. "A novel discrete model for granular material incorporating rolling resistance", *Computers and Geotechnics*, 32(5), pp. 340-357, 2005. <https://doi.org/10.1016/j.compgeo.2005.05.001>
- [33] Jiang, M. J., Yu, H. S., Harris, D. "Bond rolling resistance and its effect on yielding of bonded granulates by DEM analyses", *International Journal for Numerical and Analytical Methods in Geomechanics*, 30(8), pp. 723-761, 2006. <https://doi.org/10.1002/nag.498>
- [34] Jiang, M. J., Konrad, J. M., Leroueil, S. "An efficient technique for generating homogeneous specimens for DEM studies", *Computers and Geotechnics*, 30(7), pp. 579-597, 2003. [https://doi.org/10.1016/S0266-352X\(03\)00064-8](https://doi.org/10.1016/S0266-352X(03)00064-8)
- [35] Bolton, M. D., Gui, M. W., Garnier, J., Corte, J. F., Bagge, G., Laue, J., Renzi, R. "Centrifuge cone penetration tests in sand", *Géotechnique*, 49(4), pp. 543-552, 1999. <https://doi.org/10.1680/geot.1999.49.4.543>
- [36] Jiang, M. J., Yu, H. S., Harris, D. "Discrete element modelling of deep penetration in granular soils", *International Journal for Numerical and Analytical Methods in Geomechanics*, 30(4), pp. 335-361, 2006. <https://doi.org/10.1002/nag.473>
- [37] Dayal, U., Allen, J. H. "The Effect of Penetration Rate on the Strength of Remolded Clay and Sand Samples", *Canadian Geotechnical Journal*, 12(3), pp. 336-348, 2011. <https://doi.org/10.1139/t75-038>